Numerical Study on Blast Mitigation by a Water Mist: Impact of the Mean Droplet Diameter and Volume Fraction

J. X. Zhao, S. H. Liu, W. X. Yu and L. Jiang[†]

School of Mechanical Engineering, Nanjing University of Science and Technology, Nanjing 210094, China

†Corresponding Author Email: ljiang@njust.edu.cn

ABSTRACT

The ability of water mist to mitigate blast loads has been widely recognized. However, the effects of the mean droplet diameter and volume fraction of water mist on the blast mitigation effect and underlying mechanisms have not been comprehensively examined. In this study, a three-dimensional numerical simulation based on the Euler-Lagrangian approach was carried out to study the dissipation process of blast wave energy and momentum by water mist, as well as the impact of varying mean droplet diameters (255-855 μm) and volume fractions (2.4×10^{-3}-5.4×10^{-3}) on blast mitigation. The numerical model incorporates interphase mass, momentum, and energy exchanges, as well as droplet breakup and size distribution. The results showed that the most efficient transfer of momentum and energy between the blast wave and water mist occurred at the air/water mist interface. Subsequently, the efficiency of momentum and energy transfer decreased as the blast wave propagated within the water mist due to the blast wave mitigation. The reduction in the mean droplet diameter and the increase in the volume fraction result in an increase in both the total the surface area and number of water droplets, thereby enhancing the efficiency of energy and momentum absorption by droplets and improving their ability to mitigate blasts.

1. INTRODUCTION

Accidental detonations of energetic materials pose a significant hazard to human life, infrastructure, and equipment. Examples include the use of improvised explosive devices by terrorists targeting civilians, as well as accidental explosions during storage and transportation of energetic materials (Rigby et al., 2020; Valsamos et al., 2021). The detonation of energetic materials generates a significant number of high-temperature and high-pressure detonation products, which exert a strong force on the surrounding air to form a blast wave that travels through the surrounding air at supersonic speeds. The blast wave induces an abrupt surge in air pressure, velocity, and temperature, which can cause severe destruction.

To mitigate blast loads, various studies have evaluated the mitigation effect of materials such as solid particles (Theofanous & Chang, 2017; Pontalier et al., 2018; Pontalier et al., 2018; Sugiyama et al., 2019), water (Bornstein et al., 2015; Chen et al., 2015; Jiba et al., 2018; Bornstein et al., 2019; Kong et al., 2019; Schunck et al., 2020; Hai-bin et al., 2021) and foam (Liverts et al., 2015)

on blast loads. The use of water as a blast mitigation strategy offers several advantages: 1) Water is an inexpensive, easily collectible or storable, and environmentally nonpolluting resource (Shibue et al., 2022). 2) As a fluid, water can effectively absorb energy released during an explosion by converting it into kinetic energy (Tamba et al., 2021). 3) With its high latent heat of 2.25 MJ/kg, water can effectively absorb the heat generated by an explosion through evaporation (Ananth et al., 2012; Kong et al., 2019; Sugiyama et al., 2023). There are three primary methods for utilizing water to mitigate blast loads: immersing the explosive in a container filled with water (Q. et al., 2018; Hai-bin et al., 2021; Tamba et al., 2021), constructing a water wall or sheet to impede the propagation of detonation products and blast waves (Meekunnasombat et al., 2006; Chen et al., 2015; Cheng et al., 2005; Jeon & Eliasson, 2017), and employing water mist to reduce blast loads (Willauer et al., 2009a; Jourdan et al., 2010; Chauvin et al., 2011; Chauvin et al., 2016; Jiba et al., 2018; Kong et al., 2019; Schunck et al., 2020). In comparison to the first two techniques, the utilization of water mist provides a greater surface area for enhanced heat absorption efficiency and can serve as an effective

NOMENCLATURE

a	radius of parent droplet	Sh	Sherwood number
A_d	droplet surface area	S_m	mass source term
B_m	Spalding mass number	S_M	momentum source term
C_d	drag coefficient	S_{Yi}	species source term
$c_{p,g}$	gas mixture specific heat	t	time
$c_{p,d}$	droplet heat capacity	Ta	Taylor number
D_{im}	gas mixture diffusivity coefficient	T_d	droplet temperature
$\bar{d}$	mean droplet diameter	T_g	gas phase temperature
E_g	total energy for gas phase	u_d	droplet velocity
F_{drag}	drag force exerted on the droplet	V_g	gas phase velocity vector
h	convective heat transfer coefficient	We_d	droplet Weber number
h_d	latent heat of water	X_{liq}	mole fraction of the liquid
k_c	mass transfer coefficient	X_s	mole fraction of the vapor at the droplet surface
k_g	gas mixture phase thermal conductivity	Y_∞	vapor mass fraction in the ambient gas phase
$\dot{m}_d$	evaporation rate of a single droplet	T_g	gas phase temperature
n	size distribution parameter	Yi	mass fraction of the ith species
M_{ed}	averaged molecular weight of the gas mixture of air and water vapor	Y_s	vapor mass fraction at the surface
N_{dc}	number of droplets per unit volume of gas	Λ	Kelvin-Helmholtz wavelength
Nu	Nusselt number	μ_g	gas phase dynamic viscosity
Oh	Ohnesorge number	μ_d	droplet dynamic viscosity
p_g	gas phase pressure	ρ_g	gas phase density
Pr	Prandtl number of the gas phase	σ	surface tension
P_{sat}	saturated vapor pressure	τ	viscous stress tensor
$\dot{Q}_c$	sensible heat transfer rate	τ_b	droplet breakup time
$\dot{Q}_{lat}$	latent heat transfer rate	τ_r	droplet relaxation time
Re	Reynolds number	Ω	maximum wave growth rate
Sc	Schmidt number	Yi	mass fraction of the ith species
S_e	energy source term		

means of fire suppression (Jenft et al., 2014). Extensive research has demonstrated the potential of water mist for blast mitigation. For example, the U.S. Naval Research Laboratory (NRL) evaluated the mitigation efficiency of water mist on blast loads in a bombproof chamber, where trinitrotoluene (TNT) charges weighing 0.9 kg, 2.2 kg and 3.2 kg were detonated successively. The experimental results indicated that water mist with a Sauter mean diameter (SMD) of 50 μm reduced quasi-static pressure by 40%, 47% and 40% respectively, while also decreasing the initial overpressure and impulse (Bailey et al., 2006). Subsequently, experiments were conducted at NRL using heavier charges. The experimental results demonstrated that when water mist with a Sauter mean diameter (SMD) of 54 μm and a water mass fraction of 70 g/m^3 was applied, the impulse, initial overpressure, and quasi-static pressure generated by 22.7 kg of TNT were reduced by 40%, 36%, and 35%, respectively (Willauer et al., 2009). Additionally, numerous other studies have demonstrated the effective mitigation of overpressure, impulses, and quasi-static pressure by water mist. The extent of this effect is dependent on both the explosive mass and the characteristics of the water mist itself (such as the volume fraction and droplet size).

To date, several studies have explored the mechanism of blast mitigation using water mist. When the energetic material is detonated, the secondary reaction of the detonation product releases additional energy. For example, the detonation products of the TNT charge are rich in carbon (C) and carbon monoxide (CO). The secondary reaction of these products can release twice the energy of the detonation wave (Ferguson et al., 1999). If energetic material is surrounded by water droplets, then the secondary reaction of the detonation products will be quenched by the water droplets (Jiba et al., 2018; Schunck et al., 2020). For example, Schunck et al. found that when a charge was detonated inside water mist, the mitigation effect of the water mist on the blast load was better than that outside water mist. These researchers concluded that this was caused by the water droplets quenching the secondary reaction of the detonation products (Schunck et al., 2020). Similarly, Zetu et al. found that water mist could inhibit the expansion of the explosive fireball during the secondary reaction (Jiba et al., 2018). Yuta Sugiyama et al. quantitatively studied the energy absorbed by water droplets surrounding a charge and found that drag force and convective heat transfer were the primary blast mechanisms (Sugiyama et al., 2022). If an energetic material is detonated outside the water mist, then the blast mitigation is primarily attributed to droplets that diminish the intensity of the blast wave. For example, Huang and Zhang conducted one-dimensional numerical simulations based on the hybrid Eulerian–Lagrangian approach and concluded that momentum extraction of droplets from blast waves becomes the primary mitigation mechanism (Huang & Zhang, 2020). The greater the amount of

momentum absorbed by the droplets is, the more effective the mitigation outcome.

Another important aspect is the relationship between the mitigation effect and the properties of the water mist. Previous studies have shown that the mitigation effect of water mist on blast loads is affected by the geometric size of the water mist region, volume fraction, and droplet size. Concerning the effect of the geometric size of the water mist region, some studies have shown that a thicker water mist can enhance the mitigation effect (Sugiyama et al., 2022). However, determining the separate effects of droplet size and volume fraction remains challenging since current methods for generating water mist cannot selectively modify the volume fraction while keeping droplet size constant (Schunck et al., 2020). Consequently, experimental investigation of their impact on blast mitigation is difficult. Numerical simulation has emerged as a crucial tool in addressing this issue. Through numerical simulation, Yeom and Chang discovered that the droplet volume fraction intensifies the nonequilibrium between the droplets and gas phase, particularly in the relaxed region (Yeom & Chang, 2012). Huang and Zhang conducted a one-dimensional numerical simulation to explore the impact of the initial droplet diameter on shock attenuation. The number density of droplets was maintained at a constant value of $5 \times 10^{11}/\text{m}^3$. They considered different initial droplet diameters: 5 μm, 10 μm, 15 μm, and 20 μm, corresponding to volume fractions of 0.82×10^{-5}, 6.55×10^{-5}, 22.09×10^{-5}, and 52.36×10^{-5}, respectively. The results showed that larger droplet diameters contribute to a more pronounced attenuation effect on shock wave intensity (Huang & Zhang, 2020). To date, the potential impact of the initial droplet diameter and volume fraction on the effectiveness of water mist in mitigating blast loads, along with the underlying mechanisms driving this process, have yet to be comprehensively studied. Studying the influence of the initial droplet diameter and volume fraction on mitigating blasts could help optimize their use in different scenarios.

In this study, a three-dimensional numerical simulation based on the Euler−Lagrangian approach was carried out. The numerical model accounts for interphase mass, momentum, and energy exchanges as well as droplet breakup while also considering the size distribution for the first time. According to the results of the numerical simulation, we have acquired insights into blast wave behavior and energy and momentum transfer processes between droplets and blast waves. Furthermore, an innovative contribution of our research is that the impact of varying mean droplet diameters and volume fractions on blast mitigation was assessed while the mitigation mechanism was analyzed in terms of momentum transfer efficiency and energy transfer efficiency.

2. NUMERICAL METHOD

When a shock wave interacts with a single droplet, the droplet undergoes acceleration and atomization due to the impact of the post-shock gas. This phenomenon is referred to as secondary atomization (Guildenbecher et al., 2009). Moreover, energetic materials such as TNT release substantial heat upon detonation, which causes heating and subsequent evaporation of the droplets. Mass, momentum, and energy exchanges occur between the droplets and the blast wave. In this study, the Euler−Lagrangian approach was used to simulate the interaction between the blast wave and the water mist. The gas phase was treated as a continuum by solving the Naiver-Stokes equations, while the discrete water droplet phase was addressed using the Lagrangian method. Momentum, mass, and energy exchange between the water droplets and gas phase, as well as droplet breakup and size distribution were included in this numerical model.

2.1 Governing Equations for the Gas Phase

The gas components included oxygen, nitrogen and water vapor. The governing equations for the gas phase include the conservation laws of mass, momentum, energy, and species mass fraction, which are described as follows:

$$\frac{\partial \rho_g}{\partial t} + \nabla \cdot (\rho_g \boldsymbol{V}_g) = S_m, \tag{1}$$

$$\frac{\partial}{\partial t}(\rho_g \boldsymbol{V}_g) + \nabla \cdot (\rho_g \boldsymbol{V}_g \boldsymbol{V}_g + p_g - \boldsymbol{\tau}) = S_M, \tag{2}$$

$$\frac{\partial}{\partial t}(\rho_g E_g) + \nabla \cdot (\boldsymbol{V}(\rho_g E_g + p_g - \boldsymbol{\tau})) = S_e, \tag{3}$$

$$\frac{\partial}{\partial t}(\rho_g Y_i) + \nabla \cdot \left(\rho_g \boldsymbol{V}_g Y_i - \rho_g D_{im} \nabla Y_i\right) = S_{Y_i}. \tag{4}$$

Here, the subscript g denotes the gas phase. t, ρ_g, $\boldsymbol{V}_g$, p_g, and E_g represent the time, gas density, velocity vector, gas pressure, and total energy, respectively. $\boldsymbol{\tau}$ is the viscous stress tensor. Y_i and D_{im} are the mass fraction of the ith species and gas mixture diffusivity coefficient, respectively. D_{im} is calculated by the following:

$$Le_i = \frac{k_g}{\rho_g c_{p,g} D_{i,m}} = 1, \tag{5}$$

where k_g is the gas mixture phase thermal conductivity and $c_{p,g}$ is the gas mixture specific heat. S_m, S_M, S_e and S_{Yi} represent the mass source term, momentum source term, energy source term and species source term, respectively, as shown below:

$$S_m = -\sum_1^{N_{dc}} \dot{m}_d, \tag{6}$$

$$S_M = -\sum_1^{N_{dc}} F_{\text{drag}}, \tag{7}$$

$$S_e = -\sum_1^{N_{dc}} \left(\dot{Q}_c + \dot{Q}_{\text{lat}}\right), \tag{8}$$

$$S_{Y_i} = \begin{cases} S_m & \text{for liquid species} \\ 0 & \text{for other species.} \end{cases} \tag{9}$$

where N_{dc} is the number of droplets per unit volume of gas and $\dot{m}_d$ is the evaporation rate of a single droplet. F_{drag} is the drag force exerted on the droplet; $\dot{Q}_c$ and $\dot{Q}_{lat}$ are the sensible heat transfer rate and the latent heat transfer rate, respectively. In addition, the gas phase is treated as an ideal gas, and the equation of state of an ideal gas is given as follows:

$$p_g = \rho_g R_g T_g. \tag{10}$$

where R_g is the gas constant of 288 J/(kg K) and T_g is the temperature of the gas phase.

2.2 Governing Equations for Water Droplet Phase

A Lagrangian method was used to compute the water droplet trajectory. Each droplet was assumed to be a regular sphere with a uniform temperature. Factors such as droplet rotation and interactions between droplets, including collision and coalescence, were not accounted for. The interaction between a shock wave and a droplet lasts only a few milliseconds (Guildenbecher et al., 2009; Sharma et al., 2021), rendering gravity negligible in this study. The governing equations for water droplets include the mass equation, momentum equation, and heat transfer equation, which are described as follows:

$$\frac{dm_d}{dt} = \dot{m}_d, \tag{11}$$

$$m_d \frac{du_d}{dt} = F_{drag}, \tag{12}$$

$$c_{p,d} m_d \frac{dT_d}{dt} = \begin{cases} \dot{Q}_c & T_d < T_{vap} \\ \dot{Q}_c + \dot{Q}_{lat} & T_d \geq T_{vap} \end{cases}, \tag{13}$$

where u_d, $c_{p,d}$, T_d and T_{vap} are the droplet velocity, droplet heat capacity, droplet temperature, and evaporation temperature, respectively.

The post-shock airflow exhibits high velocity and temperature, resulting in a significantly increased droplet evaporation rate. The effect of convective flow, which transports evaporating material from the droplet surface to the gas phase, must not be overlooked. Therefore, the evaporation rate of a single droplet in Eq. (11) was estimated as follows (Miller et al., 1998; Sazhin, 2006):

$$\dot{m}_d = \begin{cases} 0 & T_d < T_{vap} \\ k_c A_d \rho_g \ln(1 + B_m) & T_d \geq T_{vap} \end{cases} \tag{14}$$

where k_c is the mass transfer coefficient; A_d is the droplet surface area; and B_m is the Spalding mass number.

The mass transfer coefficient k_c is given by the following (Ranz & Marshall, 1952):

$$Sh = \frac{k_c d_d}{D_{H_2O,m}} = 2.0 + 0.6 Re_d^{1/2} Sc^{1/3}, \tag{15}$$

where Sh is the Sherwood number; Sc is the Schmidt number, and $Sc = \mu_g/\rho_g D_{H2O,m}$, where μ_g is the dynamic viscosity; $D_{H2O,m}$ is the diffusion coefficient of vapor.

The Spalding mass number B_m is given as:

$$B_m = \frac{Y_s - Y_\infty}{1 - Y_s}, \tag{16}$$

where Y_s is the vapor mass fraction at the surface and Y_∞ is the vapor mass fraction in the ambient gas phase. Y_s was calculated by:

$$Y_s = \frac{M_d X_s}{M_d X_s + M_{ed}(1 - X_s)}, \tag{17}$$

where M_{ed} is the average molecular weight of the gas mixture of air and water vapor and X_s is the mole fraction of the vapor at the droplet surface, which is calculated using Raoult's law:

$$X_s = X_{liq} \frac{p_{sat}}{p_s}, \tag{18}$$

where X_{liq} is the mole fraction of the liquid; P_{sat} is the saturated vapor pressure and was estimated using the Antoine equation:

$$\lg p_{sat} = 7.96681 - \frac{1668.21}{T_d + 228}. \tag{19}$$

The drag force exerted on the droplet F_{drag} in Eq. (7) and Eq. (12) is expressed using the following equation:

$$F_{drag} = m_d \frac{u_g - u_d}{\tau_r}, \tag{20}$$

where τ_r is the droplet relaxation time calculated by the following:

$$\tau_r = \frac{\rho_d d_d^2}{18 \mu_g} \frac{24}{C_d Re}. \tag{21}$$

Here, C_d is the drag coefficient, and Re is the relative Reynolds number, which is defined as:

$$Re = \frac{\rho_g d_d |u_g - u_d|}{\mu_g}. \tag{22}$$

The drag coefficient C_d is expressed as (Liu et al., 1993):

$$C_d = \begin{cases} 0.424 & , Re > 1000 \\ \frac{24}{Re}\left(1 + \frac{1}{6} Re^{2/3}\right) & , Re \leq 1000 \end{cases} \tag{23}$$

The sensible heat transfer rate $\dot{Q}_c$ in Eq. (8) and Eq. (13) is calculated using the following equation:

$$\dot{Q}_c = h A_d (T_g - T_d), \tag{24}$$

where h is the convective heat transfer coefficient calculated with Nusselt number Nu as follows (Sazhin, 2006):

$$Nu = \frac{h d_d}{k_g} = \frac{\ln(1 + B_m)}{B_m}\left(2 + 0.6 Re^{1/2} Pr^{1/3}\right), \tag{25}$$
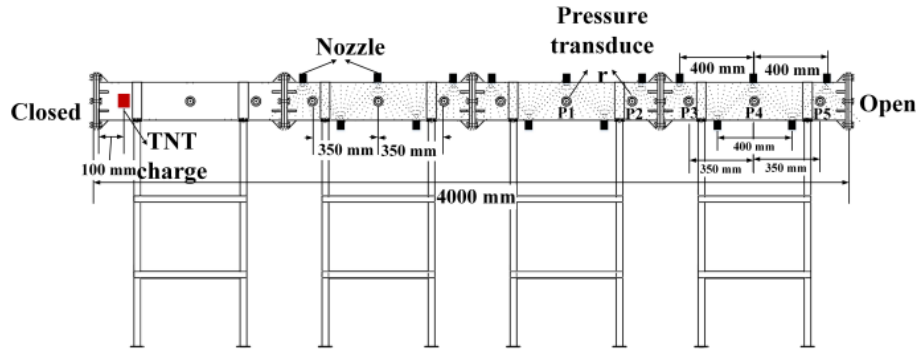
Fig. 1 Schematic diagram of the experimental setup

where Pr is the Prandtl number of the gas phase, and $Pr = c_{p,g}\mu_g/k_g$.

The latent heat transfer rate $\dot{Q}_{lat}$ in Eq. (8) and Eq. (13) is calculated by the following:

$$\dot{Q}_{lat} = -h_d \dot{m}_d, \tag{26}$$

where h_d is the latent heat of water.

2.3 Breakup Model

The wave breakup model proposed by Reitz (Reitz, 1988) was employed in this study to consider the breakup of droplets induced by a blast wave. The model assumes that the time of breakup and the size of the child droplet are related to the Kelvin-Helmholtz instability. The radius of the child droplets was proportional to the wavelength of the fastest-growing unstable surface on the parent droplet:

$$r = B_0 \Lambda, \tag{27}$$

where B_0 is a constant set equal to 0.61 based on the work of Reitz (Reitz, 1988); Λ is the wavelength which is calculated by:

$$\frac{\Lambda}{a} = 9.02 \frac{\left(1+0.45Oh^{0.5}\right)\left(1+0.4Ta^{0.7}\right)}{\left(1+0.87We_d^{1.67}\right)^{0.6}}, \tag{28}$$

where a is the radius of the parent droplet and Oh, Ta and We_d are the Ohnesorge number, Taylor number and droplet Weber number, respectively, which are calculated by:

$$Oh = \frac{\sqrt{We_d}}{Re}, \tag{29}$$

$$Ta = Oh\sqrt{We_g}, \tag{30}$$

$$We_g = \frac{\rho_g u_g a}{\sigma}, \tag{31}$$

where $We_d = \rho_d u_g a / \sigma$ and σ is the surface tension.

The rate of change of the parent droplet radius is given by:

$$\frac{da}{dt} = -\frac{(a-r)}{\tau_b}, r \leq a \tag{32}$$

where τ_b is the breakup time which is given by:

$$\tau_b = \frac{3.726 B_1 a}{\Lambda \Omega}, \tag{33}$$

where B_1 is the breakup time constant, which is recommended to set to a value of 1.73 (Liu et al., 1993). Ω is the maximum wave growth rate, which is calculated by:

$$\Omega\sqrt{\frac{\rho_g a^3}{\sigma}} = \frac{0.34+0.38We_d^{1.5}}{\left(1+Oh\right)\left(1+1.4Ta^{0.6}\right)} \tag{34}$$

2.4 Numerical Method

The numerical simulations were performed by using a density-based solver. The governing equations for the gas phase were discretized using the finite volume method. A temporal discretization method employing a second-order implicit scheme was utilized. An AUSM (Advection Upstream Splitting Method) scheme was applied for calculating convection terms. A semi-implicit trapezoidal integration was used for tracking of the droplets.

2.5 Numerical Model Validation

To validate the numerical model, a three-dimensional simulation was performed based on the the experiment conducted by Zhao et al. (2023). Figure 1 shows a schematic diagram of the experimental setup. The experiment was conducted within a blast-driven shock tube with a 4 m length and 180 mm square inner cross section. The water mist was generated using a spray system and sprayed within 1-4 m of the shock tube. The estimated volume fraction of water mist was 3.4×10^{-3}. Five piezoelectric pressure transducers (termed the P1, the P2, the P3, the P4 and P5) were flush mounted on the sidewall of the shock tube to measure blast wave overpressure within the spray region. Their respective positions are depicted in Fig. 1. A cylindrical TNT charge with a mass of 10 g was used in the experiment. One end of the shock tube was closed, and the other end was open. The charge was suspended on the central axis of the shock tube, 100 mm away from the closed end.

The droplet size distribution was determined by employing a laser light scattering analyzer, and the corresponding outcomes are illustrated in Fig. 2.

Figure 3 shows the three-dimensional computational domain, which was established based on the experimental setup. The dimensions of the computational domain were consistent with those of the shock tube. According to the
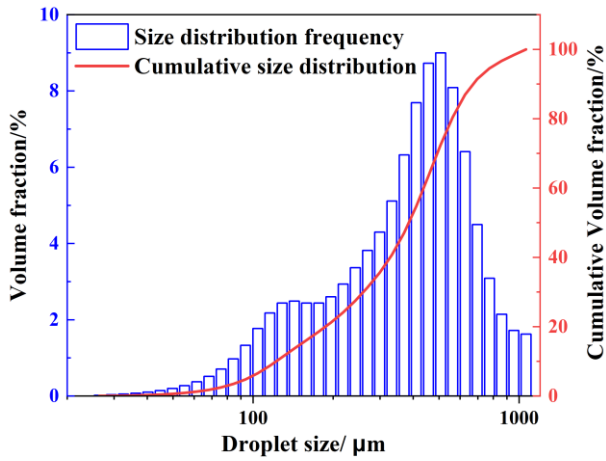
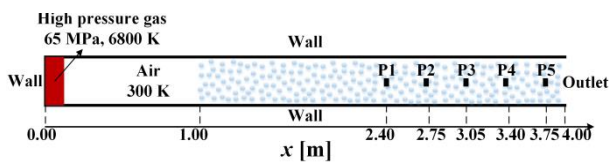**Fig. 2 Size distributions of water droplets**

Table 1 Physical properties for the gas phase and droplet

Symbol	Value
k_g	0.0454 W/(m · k)
μ_g	1.72×10⁻⁵ Pa · s
μ_d	0.001003 Pa · s
$c_{p,\,g}$	1007 J/(kg · K)
$c_{p,\,d}$	4182 J/(kg · K)
h_d	2263073 J/kg
σ	0.072 N/m
T_{g0}	300 K
T_{d0}	300 K
T_{vap}	284 K

Fig. 3 Schematic diagram of the computational domain and initial conditions

pressurized bubble method(PBM) proposed by Blanc et al (Blanc et al., 2018), an air region with a pressure of 65 MPa and temperature of 6800 K was introduced at the left end wall of the computational domain to simulate detonation products resulting from a 10 g TNT charge. The accuracy of PBM in simulating the propagation of blast waves in computational fluid dynamics (CFD) has been validated by Mohotti et al. (2023). The water droplets were uniformly distributed within the range of $1 \le x \le 4$ m in the computational domain. The computational grid employed in this study had a constant cell width of 5 mm. We employed an outflow boundary condition at the shock tube outlet and employed a wall boundary for the left-end wall as well as both sidewalls. As depicted in Fig. 3, P1-P5 represent the locations where pressure values were recorded during the numerical simulation.

In previous numerical simulation studies, the assumption of droplets having identical diameters has been commonly adopted. Hence, for a more precise prediction of this issue, we employed an identical droplet size distribution as that utilized in the experiment. The Rosin–Rammler expression is a practical way to depict the size distribution of droplets in liquid sprays. The Rosin–Rammler distribution can be written as:

$$Y = 1 - \exp\left[-\left(\frac{d}{\bar{d}}\right)^n\right], \tag{35}$$

where Y is the volume fraction smaller than a given diameter d and $\bar{d}$ is the mean diameter. The value of $\bar{d}$ is 455 μm which is determined by observing that it corresponds to the point at which Y equals 0.632. n is the size distribution parameter which is calculated by the following:

$$n = \frac{\ln\left[-\ln(1-Y)\right]}{\ln(d / \bar{d})} \tag{36}$$

By substituting the measured droplet size distribution presented in Fig. 2 into Eq. (36), we can obtain values for and find an average of $n=2.1$.

The physical properties for the gas phase and droplet associated with the present numerical simulation are listed in Table 1.

Figure 4 shows the comparison between the experimental and numerical pressure histories under both water mist presence and absence. Zero time was defined as when the blast wave reached the first pressure transducer the P1. The presence of water mist resulted in a reduction in both the initial overpressure, which was observed on all transducers. The overpressure was reduced by 50% to 78%, thereby demonstrating the remarkable mitigation efficacy of water mist in attenuating blast waves. The simulated pressure histories at P1-P3 exhibited good agreement with the experimental results in both cases with and without water mist. However, in the presence of water mist, the peak overpressure of the simulated pressure histories at P4 and P5 were larger than that of the experimental results, and their arrival times were later (Fig. 4. h and Fig. 4. j).

The differences between the experimental and numerical results stem from two factors. First, in the experiment, partial water droplets were attached to the wall of the shock tube, whereas in the numerical simulation, all water droplets were suspended in air. Second, in the numerical situation, the droplets were uniformly distributed in the computational domain, which deviates from the experimental conditions. Nevertheless, in general, the experimental results and numerical simulation results still maintain a high consistency.

3. THE BEHAVIOR OF BLAST WAVES AND WATER DROPLETS

To gain insight into the behavior of the blast wave, Fig. 5 presents the *x-t* diagram of the overpressure. The dotted line in Fig. 5 represents the air/water mist interface. Zero time is defined as when the numerical calculation starts.
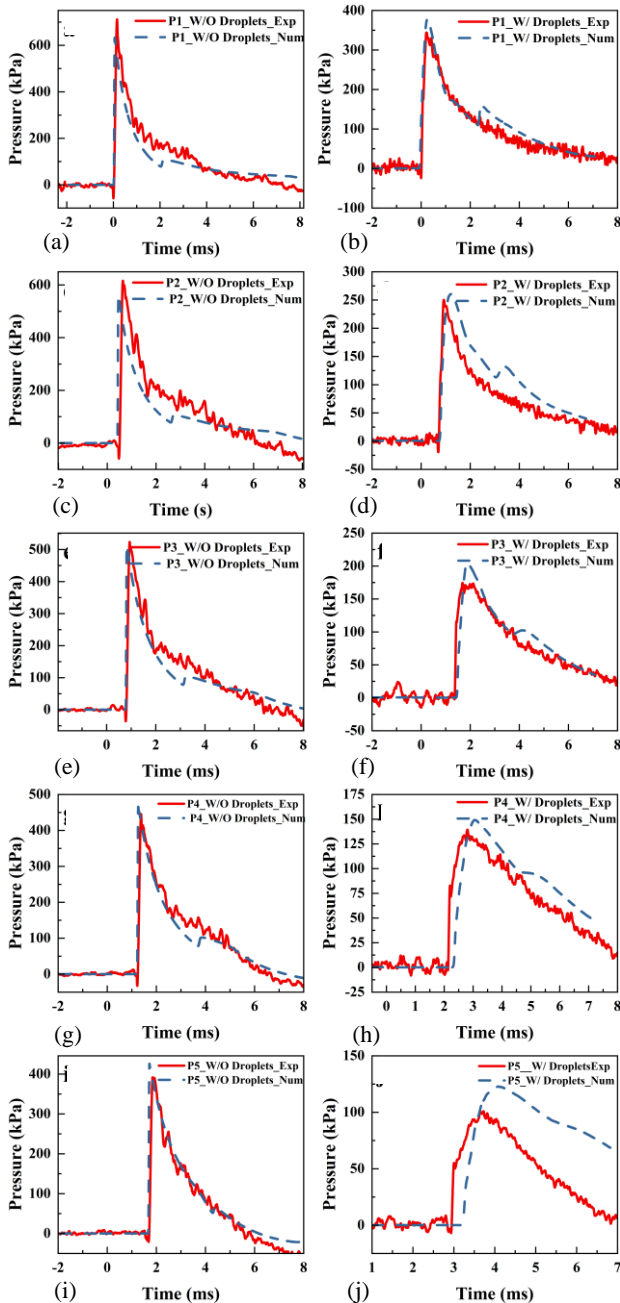
Fig. 4 Comparison between experimental and numerical pressure histories with and without water mist
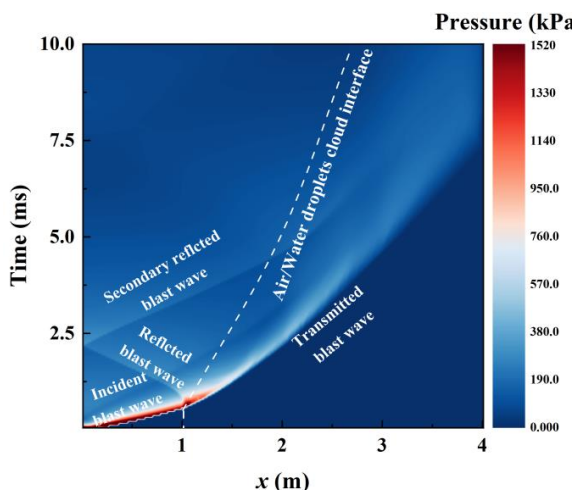

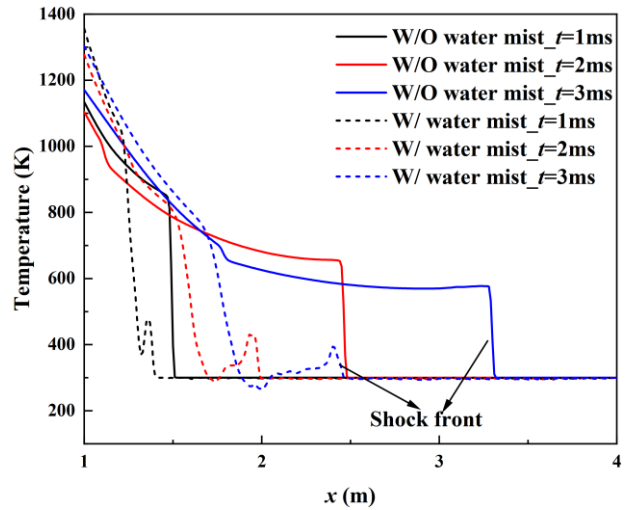**Fig. 5 *x-t* diagram of the overpressure**

Fig. 6 Comparisons of the temperature for the gas phase in the presence and absence of water mist at *t*=1 ms, 2 ms, and 3 ms

The incident blast wave reached the interface at *t*=0.5 ms, where it underwent transmission and reflection to generate a transmitted and reflected blast waves, respectively. The transmitted blast wave propagated along the +*x* direction within the water mist, while the reflected blast wave traveled along the -*x* direction. When the reflected blast wave reached the left end wall of the shock tube, a secondary reflected blast wave was formed and propagated along the +*x* direction. However, we did not observe a secondary reflected blast wave in the experimental pressure histories (Fig. 4). This discrepancy can be attributed to differences in droplet distribution at the air/water mist interface between the experiment and simulation. In the numerical situation, the droplets were uniformly distributed at the air/water mist interface, forming a dense "droplet wall" parallel to the incident blast wave. However, in the experimental situation, water mist was generated by nozzles, resulting in an oblique air/mist interface. In addition, the droplets were very sparse and unevenly distributed at the interface, resulting in a complete reflected blast wave that could not be formed.

Figure 6 shows the comparisons of the temperature for the gas phase along the +*x* direction in the presence and absence of water mist at *t*=1 ms, 2 ms, and 3 ms. The blast wave induced an abrupt surge in the gas phase temperature, while the water mist significantly reduced the temperature of the gas phase behind the shock front. Furthermore, as the transmitted blast wave propagated, a continuous decrease in temperature was observed. It was also noted that the position of the shock front in the case of water mist is observed to be located more posteriorly compared to that in the absence of water mist. This observation implies that the velocity of the blast wave is decelerated by the introduction of water mist.

Figure 7 shows the comparisons of the velocity for the gas phase along the +*x* direction in the presence and absence of water mist at *t*=1 ms, 2 ms, and 3 ms. It is evident that the blast wave induced an abrupt surge in gas phase velocity. The presence of water mist leads to a reduction in the velocity of the gas phase behind the shock
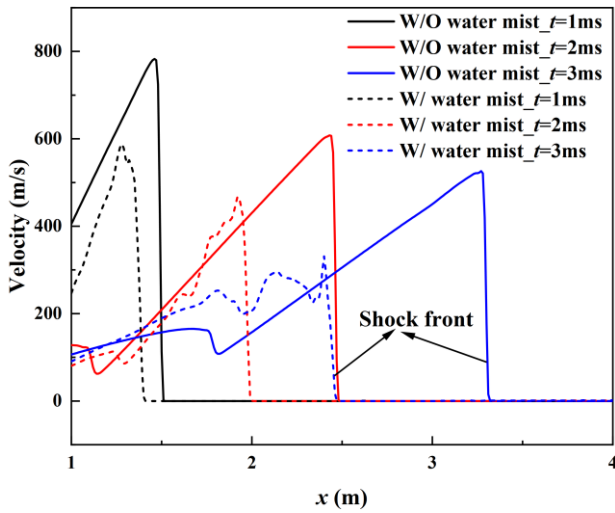
Fig. 7 Comparisons of the velocity for the gas phase in the presence and absence of water mist at *t*=1 ms, 2 ms, and 3 ms
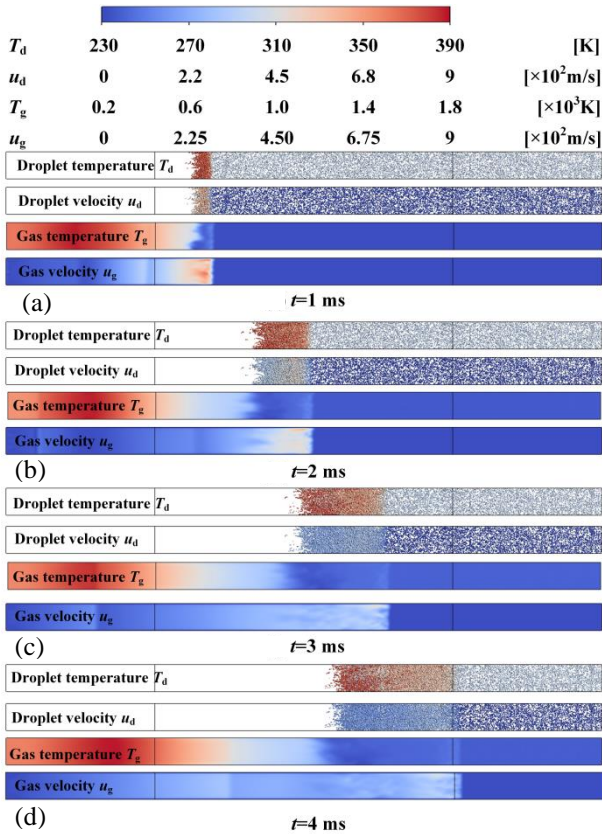

Fig. 9 Peak overpressure at P1-P5 with four different mean droplet diameters

a significant increase in the number of the child droplets. It can be observed from the gas phase temperature distribution diagram that the heat accumulated on the left side of the air/water mist interface. This indicated that most of the heat of detonation products was obstructed by the water mist and could not be transferred into the water mist region.

4. THE EFFECT OF MEAN DROPLET DIAMETER AND VOLUME FRACTION

4.1 Effect of the Mean Droplet Diameter

This section will assess the effect of the mean droplet diameter $\bar{d}$ on blast mitigation. The droplets had initial diameters of 255 μm, 455 μm, 655 μm, and 855 μm, while the volume fraction of the water mist remained fixed at a value of 3.4×10^{-3}. Figure 9 shows the peak overpressure at P1-P5 with four different mean droplet diameters. The decrease in mean droplet diameter resulted in a corresponding reduction in peak overpressure, suggesting that the blast mitigation effect can be enhanced by reducing droplet size.

Figure 10 illustrates the sensible heat transfer rate $\dot{Q}_c$ (a), latent heat transfer heat rate $\dot{Q}_{lat}$ (b), energy source term S_e(c) and momentum source term S_M (d) with four different mean droplet diameters. At t=0.5 ms, the incident blast wave reached the air/water mist interface, initiating momentum and energy exchange between the water droplets and gas phase. The high-speed and high-temperature post-shock airflow started to transfer momentum and heat to the droplets through drag force and convective heat transfer. Consequently, $\dot{Q}_c$, $\dot{Q}_{lat}$, S_e and S_M rapidly increase at t=0.5 ms. According to Eq. (7), S_M is equal to the sum of the drag force F_{drag} exerted on all droplets, while F_{drag} is positively correlated with the velocity difference between the gas phase and the droplets according to Eq. (20). In addition, $\dot{Q}_c$ and $\dot{Q}_{lat}$ are positively correlated with the convective heat transfer coefficient h and evaporation rate of the droplet according to Eq. (24) and Eq. (26). However, as the transmitted blast

Fig. 8 The velocity and temperature distributions of both the droplets and gas phase at t=1 ms (a), t=2 ms (b), t=3 ms (c), and t=4 ms (d).

front. As the transmitted blast wave propagates, there is a gradual decrease in the velocity of the gas phase behind the shock front.

Figure 8 displays the velocity and temperature distributions of both the droplets and gas phase at *t*=1 ms, *t*=2 ms, *t*=3 ms, and *t*=4 ms. The droplets were accelerated and heated by the post-shock airflow, with continuous momentum absorption and energy absorption. Behind the shock front, water droplets underwent breakup, leading to
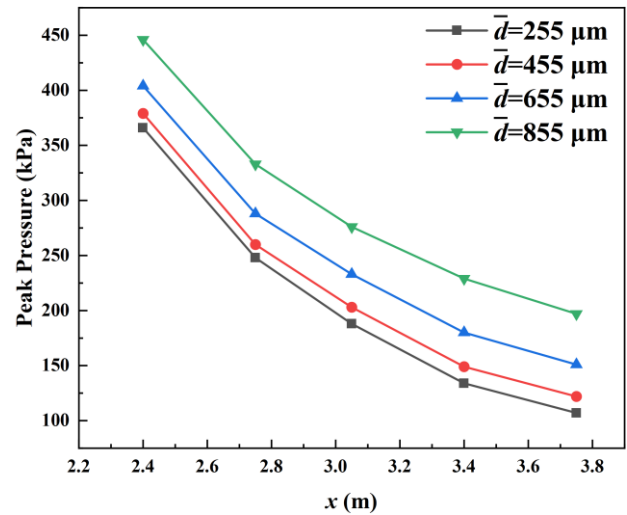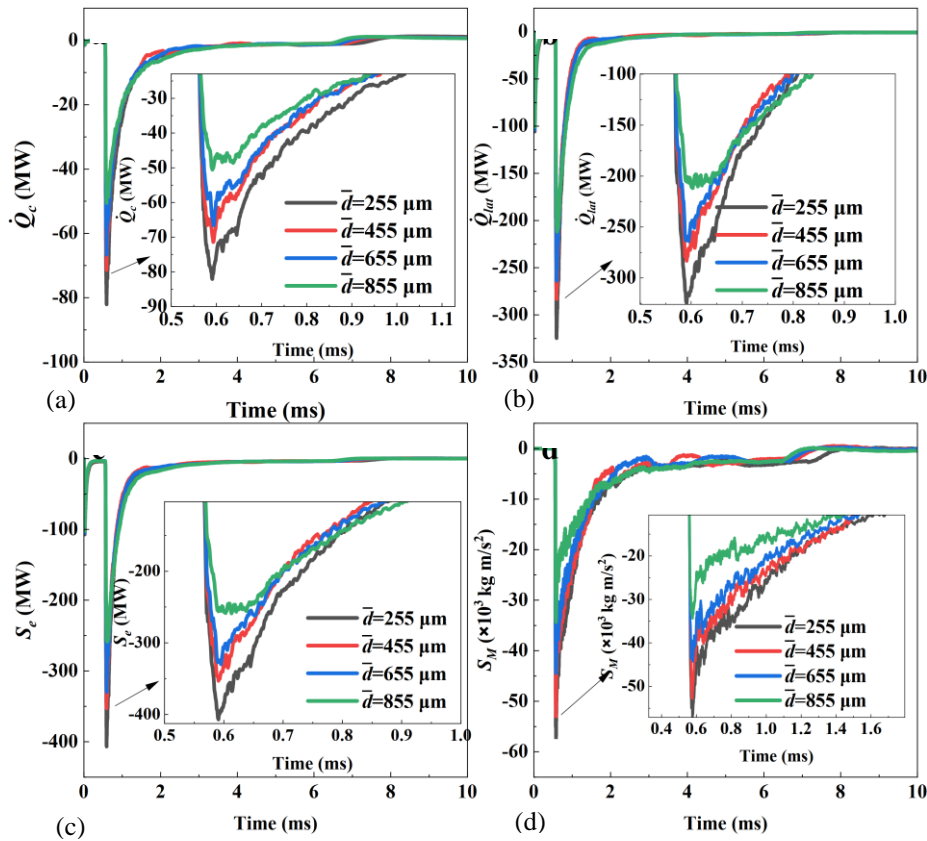
Fig. 10 The sensible heat transfer rate(a), latent heat transfer heat rate(b), energy source term S_e (c) and momentum source term S_M (d) with four different mean droplet diameters

wave propagated, the temperature and velocity of the airflow behind it decreased continuously (as shown in Fig. 6 and Fig. 7), resulting in a decrease in the momentum transfer efficiency, convective heat transfer efficiency and evaporation rate of the droplets. Therefore, $\dot{Q}_c$, $\dot{Q}_{lat}$, S_e and S_M decreased rapidly after reaching their peak.

It can also be noted from Fig. 10 that the reduction in droplet diameter significantly enhanced the efficiency of sensible heat transfer, latent heat transfer, and momentum transfer. According to the expressions of $\dot{Q}_c$ and $\dot{Q}_{lat}$ (Eq. (24) and Eq. (26)), $\dot{Q}_c$ and $\dot{Q}_{lat}$ are directly proportional to the surface area of droplets. A decrease in droplet diameter significantly increases the total surface area of the water and the number of droplets in the computational domain (Adiga et al., 2009). Therefore, the increase in total droplet surface area was the underlying cause of enhanced efficiency in both latent heat absorption and sensible heat absorption. In terms of the momentum source term S_M, as shown in Fig. 10.d, S_M increases as the mean droplet diameter decreases. The main reason for this phenomenon is the increase in the number of droplets per unit volume of gas.

4.2 Effect of Volume Fraction

This section focuses on the effect of the volume fraction of water mist on blast mitigation and the exchange of energy and momentum. The volume fractions of water mist were $2.4×10^{-3}$, $3.4×10^{-3}$, $4.4×10^{-3}$ and $5.4×10^{-3}$ with a fixed mean droplet diameter of 455 μm. The distribution of peak overpressure at P1-P5 with four different volume
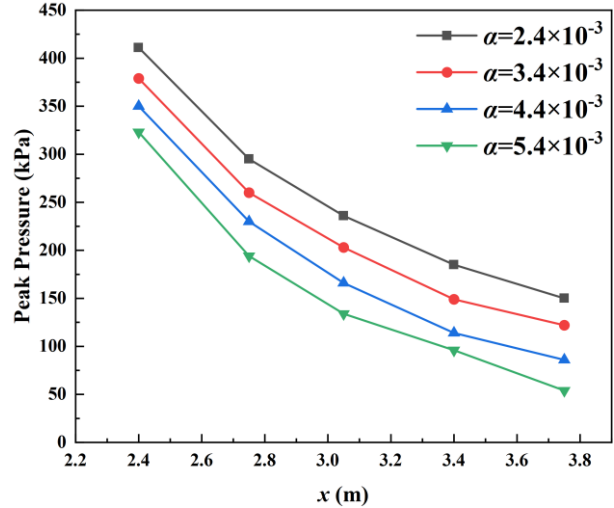

Fig. 11 Peak overpressure at P1-P5 with four different volume fractions

fractions is illustrated in Fig. 11. It is evident that the peak pressure decreases as the volume fraction increases, indicating that the blast mitigation effect can be enhanced by increasing volume fractions. Figure 12 illustrates the sensible heat transfer rate $\dot{Q}_c$ (a), latent heat transfer heat rate $\dot{Q}_{lat}$ (b), energy source term S_e (c) and momentum source term S_M (d) with four different volume fractions. It is evident that an increase in the volume fraction significantly enhances the efficiency of sensible heat transfer, latent heat transfer, and momentum transfer.
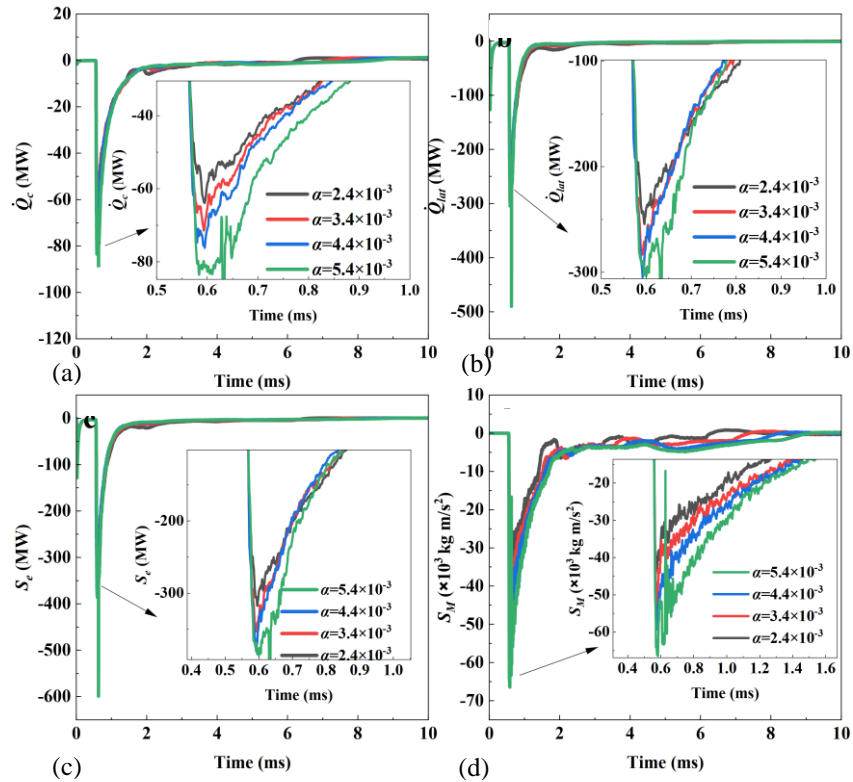
Fig. 12 The sensible heat transfer rate (a), latent heat transfer heat rate (b), energy source term S_e(c) and momentum source term S_M(d) with four different volume fractions
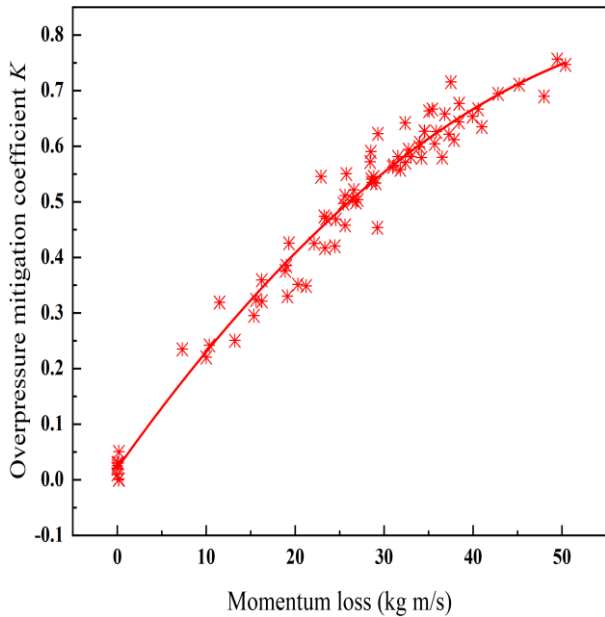

Fig. 13 The momentum loss from the gas phase versus the overpressure mitigation coefficient K
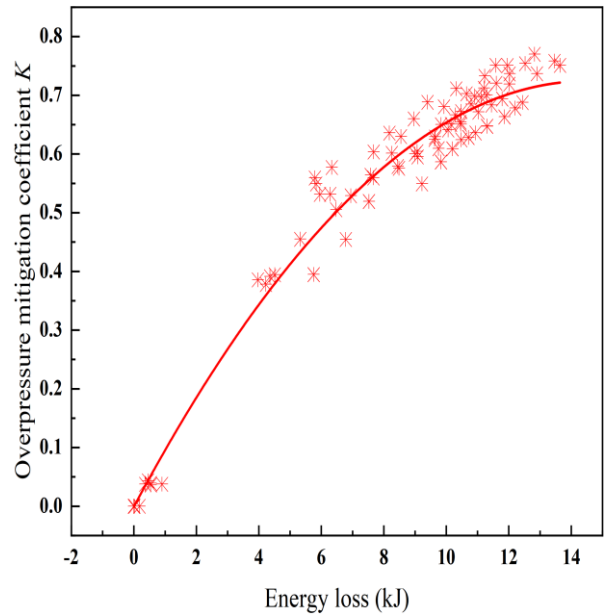

Fig. 14 The energy loss from the gas phase versus the overpressure mitigation coefficient K

Once again, this was attributed to the higher volume fraction, which led to an increased number of droplets and a greater liquid surface area within the computational domain, thereby enhancing the efficiency of the sensible heat transfer, latent heat transfer, and momentum transfer.

To investigate the correlation between blast mitigation effectiveness and the overall transfer of energy and momentum, we conducted calculations on the overpressure mitigation coefficient K, as well as the total momentum and energy losses. These calculations were carried out when the shock front reached specific positions at x=1.3, 1.6, 1.9, 2.2, 2.5, 2.8, 3.1, 3.4, 3.7, and 4 m, considering all calculation conditions. The momentum loss and energy loss were determined by integrating the respective values of S_M and S_e over time. The overpressure mitigation coefficient K is calculated by:

$$K = \frac{P_{W/O} - P_{W/}}{P_{W/O}} \tag{37}$$

where $P_{W/O}$ is the peak overpressure without water mist and $P_{W/}$ is the peak overpressure with water mist.

Figures 13 and 14 present the momentum loss and energy loss from the gas phase versus the K, respectively. The red curves shown in Figs 13 and 14 are approximate curves, and they were obtained by fitting a quadratic polynomial to the data. The coefficient of determination, R^2, for these curves is 0.97 and 0.93, respectively. This value indicates how well the fitted model represents the observed data. In this case, an R^2 value close to 1 suggests that the fitted model fits the data quite well. Regarding the relationship between momentum loss or energy loss and K, importantly, the change in K does not follow a linear trend but rather shows a quadratic trend. When there is an increase in momentum loss or energy loss, K also increases. This suggests that as the droplets acquire more energy and momentum from the gas phase, they become more effective in attenuating the blast wave.

5. CONCLUSION

The objective of this study was to investigate the dissipation mechanism of blast wave energy and momentum through water mist, as well as the influence of droplet diameter and volume fraction on blast mitigation effectiveness. A three-dimensional numerical simulation based on the Euler-Lagrangian approach was conducted to investigate details regarding the propagation of blast waves and interphase interactions. The numerical model accounts for interphase mass, momentum, and energy exchanges as well as droplet breakup and size distribution. The present numerical model was validated through comparisons with the experimental and numerical pressure histories. According to the numerical results, the most efficient transfer of momentum and energy between the blast wave and the water mist occurred at their contact interface. As the blast wave propagated, the blast wave was mitigated by water mist through momentum extraction, evaporation and convective heat transfer. Due to the mitigation of the blast wave, the velocity and temperature of the post-shock airflow continuously decrease, resulting in a reduction in momentum and energy transfer efficiency between the blast wave and droplets.

Finally, the impact of varying droplet diameters and volume fractions on blast mitigation was assessed. Reducing the droplet diameter and increasing the volume fraction led to a higher total surface area and a greater number of water droplets, ultimately enhancing the efficiency of energy and momentum absorption by the droplets and improving their ability to mitigate blast.

ACKNOWLEDGMENTS

CONFLICT OF INTEREST

The authors have no conflicts to disclose.

AUTHOR CONTRIBUTION

J. X. Zhao: Conceptualization (lead), Investigation (equal), Software (lead), Data Curation (equal), Original Draft Preparation (lead); **S. H. Liu**: Investigation (equal), Data Curation (equal); **W. X. Yu**: Investigation (equal); **L. Jiang**: Supervision (lead);Writing-Review & Editing (lead).

REFERENCES

Adiga, K. C., Willauer, H. D., Ananth, R., & Williams, F. W. (2009). Implications of droplet breakup and formation of ultra fine mist in blast mitigation. *Fire Safety Journal*, *44*(3), 363-369. https://doi.org/10.1016/j.firesaf.2008.08.003

Ananth, R., Willauer, H. D., Farley, J. P., & Williams, F. W. (2012). Effects of Fine Water Mist on a Confined Blast. *Fire Technology*, *48*(3), 641-675. https://doi.org/10.1007/s10694-010-0156-y

Bailey, J. L., Farley, J. P., Williams, F. W., Lindsay, M. S., & Schwer, D. A. (2006). Blast Mitigation Using Water Mist. *NRL Report*, 6180-06. https://doi.org/10.1016/j.ijimpeng.2014.08.014

Blanc, L., Herrera, S. S., & Hanus, J. L. (2018). Simulating the blast wave from detonation of a charge using a balloon of compressed air. *Shock Waves*, *28*(4), 641-652. https://doi.org/10.1007/s00193-017-0774-0

Bornstein, H., Phillips, P., & Anderson, C. (2015). Evaluation of the blast mitigating effects of fluid containers. *International Journal of Impact Engineering*, *75*, 222-228. https://doi.org/10.1016/j.ijimpeng.2014.08.014

Bornstein, H., Ryan, S., & Mouritz, A. P. (2019). Evaluation of blast protection using novel-shaped water-filled containers: Experiments and simulations. *International Journal of Impact Engineering*, *127*, 41-61. https://doi.org/10.1016/j.ijimpeng.2019.01.006

Chauvin, A., Daniel, E., Chinnayya, A., Massoni, J., & Jourdan, G. (2016). Shock waves in sprays: numerical study of secondary atomization and experimental comparison. *Shock Waves*, *26*(4), 403-415. https://doi.org/10.1007/s00193-015-0593-0

Chauvin, A., Jourdan, G., Daniel, E., Houas, L., & Tosello, R. (2011). Experimental investigation of the propagation of a planar shock wave through a two-phase gas-liquid medium. *Physics of Fluids*, *23*(11), 13, Article 113301. https://doi.org/10.1063/1.3657083

Chen, L., Zhang, L., Fang, Q., & Mao, Y. M. (2015). Performance based investigation on the construction of anti-blast water wall. *International Journal of Impact Engineering*, *81*, 17-33. https://doi.org/10.1016/j.ijimpeng.2015.03.003

Cheng, M., Hung, K. C., & Chong, O. Y. (2005). Numerical study of water mitigation effects on blast wave. *Shock Waves*, *14*(3), 217-223. https://doi.org/10.1007/s00193-005-0267-4

Ferguson, R. E., Kuhl, A. L., & Oppenheim, A. K. (1999). Combustion of TNT products in a confined explosion. United States. https://www.osti.gov/servlets/purl/9375.

Guildenbecher, D. R., López-Rivera, C., & Sojka, P. E. (2009). Secondary atomization. *Experiments in Fluids*, *46*(3), 371. https://doi.org/10.1007/s00348-008-0593-2

Hai-bin, X., Long-kui, C., De-zhi, Z., Fang-ping, Z., Zhao-wu, S., Wen-xiang, L., & Sheng-hong, H. (2021). Mitigation effects on the reflected overpressure of blast shock with water surrounding an explosive in a confined space. *Defence Technology*, *17*(03), 1071-1080. https://doi.org/https://doi.org/10.1016/j.dt.2020.06.026

Huang, Z. W., & Zhang, H. W. (2020). On the interactions between a propagating shock wave and evaporating water droplets. *Physics of Fluids*, *32*(12), 14, Article 123315. https://doi.org/10.1063/5.0035968

Jenft, A., Collin, A., Boulet, P., Pianet, G., Breton, A., & Muller, A. (2014). Experimental and numerical study of pool fire suppression using water mist. *Fire Safety Journal*, *67*, 1-12. https://doi.org/10.1016/j.firesaf.2014.05.003

Jeon, H., & Eliasson, V. (2017). Shock wave interactions with liquid sheets. *Experiments in Fluids*, *58*(4). https://doi.org/10.1007/s00348-017-2300-7

Jiba, Z., Sono, T. J., & Mostert, F. J. (2018). Implications of fine water mist environment on the post-detonation processes of a PE4 explosive charge in a semi-confined blast chamber. *Defence Technology*, *14*(5), 366-372. https://doi.org/10.1016/j.dt.2018.05.005

Jourdan, G., Biamino, L., Mariani, C., Blanchot, C., Daniel, E., Massoni, J., Houas, L., Tosello, R., & Praguine, D. (2010). Attenuation of a shock wave passing through a cloud of water droplets. *Shock Waves*, *20*(4), 285-296. https://doi.org/10.1007/s00193-010-0251-5

Kong, X. S., Zhou, H., Zheng, C., Liu, H. B., Wu, W. G., Guan, Z. W., & Dear, J. P. (2019). An experimental study on the mitigation effects of fine water mist on confined-blast loading and dynamic response of steel plates. *International Journal of Impact Engineering*, *134*. https://doi.org/https://doi.org/10.1016/j.ijimpeng.2019.103370

Liu, A. B., Mather, D., & Reitz, R. D. (1993). Modeling the Effects of Drop Drag and Breakup on Fuel Sprays. *Sae Paper*, *93*, https://doi.org/10.4271/930072.

Liverts, M., Ram, O., Sadot, O., Apazidis, N., & Ben-Dor, G. (2015). Mitigation of exploding-wire-generated blast-waves by aqueous foam. *Physics of Fluids*, *27*(7), 076103. https://doi.org/10.1063/1.4924600

Meekunnasombat, P., Oakley, J. G., Anderson, M. H., & Bonazza, R. (2006). Experimental study of shock-accelerated liquid layers. *Shock Waves*, *15*(6), 383-397. https://doi.org/10.1007/s00193-006-0039-9

Miller, R. S., Harstad, K., & Bellan, J. (1998). Evaluation of equilibrium and non-equilibrium evaporation models for many-droplet gas-liquid flow simulations. *International Journal of Multiphase Flow*, *24*(6), 1025-1055. https://doi.org/10.1016/s0301-9322(98)00028-7

Mohotti, D., Wijesooriya, K., & Weckert, S. (2023). A simplified approach to modelling blasts in computational fluid dynamics (CFD). *Defence Technology*, *23*, 19-34. https://doi.org/10.1016/j.dt.2022.11.006

Pontalier, Q., Lhoumeau, M., Milne, A. M., Longbottom, A. W., & Frost, D. L. (2018). Numerical investigation of particle-blast interaction during explosive dispersal of liquids and granular materials. *Shock Waves*, *28*(3), 513-531. https://doi.org/10.1007/s00193-018-0820-6

Pontalier Q., Loiseau, J., Goroshin, S., & Frost, D. L. (2018). Experimental investigation of blast mitigation and particle–blast interaction during the explosive dispersal of particles and liquids. *Shock Waves*, *28*(3), https://doi.org/10.1007/s00193-018-0821-5

Ranz, W. E., & Marshall, W. R. (1952). Evaporation from drops, part I. *Chemical Engineering Progress*, *48*(3), 141-146. https://www.researchgate.net/publication/304113941_Evaporation_from_drops_part_I

Reitz, R. D. (1988). Mechanisms of atomization processes in high-pressure vaporizing sprays. *Atomization and Spray Technology*, *3*, https://www.researchgate.net/publication/234279474_Modeling_atomization_processes_in_high-pressure_vaporizing_sprays

Rigby, S. E., Lodge, T. J., Alotaibi, S., Barr, A. D., Clarke, S. D., Langdon, G. S., & Tyas, A. (2020). Preliminary yield estimation of the 2020 Beirut explosion using video footage from social media. *Shock Waves*, *30*(6), 671-675. https://doi.org/10.1007/s00193-020-00970-z

Sazhin, S. S. (2006). Advanced models of fuel droplet heating and evaporation. *Progress in Energy and Combustion Science*, *32*(2), 162-214. https://doi.org/10.1016/j.pecs.2005.11.001

Schunck, T., Bastide, M., Eckenfels, D., & Legendre, J. F. (2020). Blast mitigation by water mist: the effect of the detonation configuration. *Shock Waves*, *30*(6), 629-644. https://doi.org/10.1007/s00193-020-00960-1

Sharma, S., Pratap Singh, A., Srinivas Rao, S., Kumar, A., & Basu, S. (2021). Shock induced aerobreakup of a droplet. *Journal of Fluid Mechanics*, *929*, https://doi.org/10.1017/jfm.2021.860.

Shibue, K., Sugiyama, Y., & Matsuo, A. (2022). Numerical study of the effect on blast-wave mitigation

of the quasi-steady drag force from a layer of water droplets sprayed into a confined geometry. *Process Safety and Environmental Protection*, *160*, 491-501. https://doi.org/10.1016/j.psep.2022.02.038

Sugiyama, Y., Ando, H., Shimura, K., & Matsuo, A. (2019). Numerical investigation of the interaction between a shock wave and a particle cloud curtain using a CFD-DEM model. *Shock Waves*, *29*(4), 499-510. https://doi.org/10.1007/s00193-018-0878-1

Sugiyama, Y., Shibue, K., & Matsuo, A. (2023). The blast mitigation mechanism of a single water droplet layer and improvement of the blast mitigation effect using multilayers in a confined geometry. *International Journal of Multiphase Flow*, *159*, 11, Article 104322. https://doi.org/ARTN 10432210.1016/j.ijmultiphaseflow.2022.104322

Sugiyama, Y., Tamba, T., & Ohtani, K. (2022). Numerical study on a blast mitigation mechanism by a water droplet layer: Validation with experimental results, and the effect of the layer radius. *Physics of Fluids*, *34*(7), 19, Article 076104. https://doi.org/10.1063/5.0091959

Tamba, T., Sugiyama, Y., Ohtani, K., & Wakabayashi, K. (2021). Comparison of blast mitigation performance between water layers and water droplets. *Shock Waves*, *31*(1), 89-94. https://doi.org/10.1007/s00193-021-00990-3

Theofanous, T. G., & Chang, C. H. (2017). The dynamics of dense particle clouds subjected to shock waves. Part 2. Modeling/numerical issues and the way forward. *International Journal of Multiphase Flow*, *89*, 177-206. https://doi.org/10.1016/j.ijmultiphaseflow.2016.10.004

Valsamos, G., Larcher, M., & Casadei, F. (2021). Beirut explosion 2020: A case study for a large-scale urban blast simulation. *Safety Science*, *137*, 11, Article 105190. https://doi.org/10.1016/j.ssci.2021.105190

Willauer, H. D., Ananth, R., Farley, J. P., & Williams, F. W. (2009a). Mitigation of TNT and Destex explosion effects using water mist. *Journal of hazardous materials*, *165*(1), 1068-1073. https://doi.org/10.1016/j.jhazmat.2008.10.130

Willauer, H. D., Ananth, R., Farley, J.P., Williams, F.W., Back, G.G., Kennedy, M., O'connor, J., & Gameiro, V.M. (2009). Blast Mitigation Using Water Mist: Test Series II. https://www.researchgate.net/publication/235207991_Blast_Mitigation_Using_Water_Mist_Test_Series_II

Yeom, G. S., & Chang, K. S. (2012). Dissipation of shock wave in a gas-droplet mixture by droplet fragmentation. *International Journal of Heat and Mass Transfer*, *55*(4), 941-957. https://doi.org/10.1016/j.ijheatmasstransfer.2011.10.015

Zhao, J., Li, Q., Zhang, L., Liu, S., & Jiang, L. (2023). Experimental study on mitigation effects of water mist on blast wave. *Explosion and Shock Waves*, 1-13. https://doi.org/10.11883/bzycj-2023-0108